Band splitting induced Berry flux and intrinsic anomalous Hall conductivity in the NiCoMnGa quaternary Heusler compound

Gaurav K. Shukla,[1] Jyotirmoy Sau,[2] Vishal Kumar,[1] Manoranjan Kumar,[2] and Sanjay Singh [1,*]

[1]*School of Materials Science and Technology, Indian Institute of Technology (Banaras Hindu University), Varanasi 221005, India*

[2]*S. N. Bose National Centre for Basic Sciences, Kolkata 700098, West Bengal, India*

(Received 8 April 2022; revised 16 June 2022; accepted 5 July 2022; published 22 July 2022)

The anomalous transport properties of Heusler compounds have become a hot spot of research in recent years due to their unique band structure and possible application in spintronics. In this paper, we report the anomalous Hall effect in a polycrystalline NiCoMnGa quaternary Heusler compound by experimental means and theoretical calculations. The experimental anomalous Hall conductivity (AHC) was found to be about 256 S/cm at 10 K with an intrinsic contribution of ∼121 S/cm. The analysis of Hall data reveals the presence of both extrinsic and intrinsic contributions in the anomalous Hall effect. Our theoretical calculations show that a pair of spin-orbit coupled bands formed by the band splitting due to spin-orbit interaction at the Fermi level produces a finite Berry flux in the system that provides an intrinsic AHC of about 100 S/cm, which is in good agreement with the experiment.

DOI: 10.1103/PhysRevB.106.045131

I. INTRODUCTION

The conventional Hall effect describes the phenomenon of transverse deflection of moving charges in a current-carrying conductor placed in a magnetic field, and this effect leads to a voltage difference perpendicular to both the direction of motion of charges and the magnetic field [1]. However, in ferromagnetic materials an additional large transverse voltage drop occurs in comparison to the normal conductors, and this phenomenon is known as the anomalous Hall effect (AHE) [2–5]. So far, two kinds of mechanisms have been proposed to understand the origin of the AHE: intrinsic and extrinsic mechanisms [6–9].

In the intrinsic mechanism, the interband mixing along with spin-orbit interaction (SOI) results in an anomalous velocity of electrons perpendicular to the electric field direction [8]. Subsequently, this anomalous velocity was reformulated in terms of the Berry phase and Berry curvature of Bloch bands [5,10,11]. Berry curvature is a pseudomagnetic field in momentum space, which acts just like the magnetic field in electrodynamics [5,11,12]. The SOI has small energy in comparison to the exchange splitting energy of ferromagnets; however, the small energy of SOI can split the band dispersion near the Fermi energy, and when the Fermi energy lies in the SOI energy gap, a nonzero dissipationless Hall current arises due to the nonvanishing total flux of the Berry curvature [1,13,14]. The anomalous Hall conductivity (AHC) due to the Berry phase (the intrinsic mechanism) does not depend on the longitudinal conductivity σ_{xx} [15,16].

The external origin of the AHE, which includes the skew scattering and side jump mechanisms, is known as the extrinsic mechanism. Skew scattering is an asymmetric scattering of carriers by the impurity potential, which introduces a momentum perpendicular to both the incident wave vector **k** and magnetization M. AHC due to skew scattering is proportional to σ_{xx} [6]. Side jump is a microscopic displacement of the wave packet due to SOI coupled Bloch states under the influence of disorder potential, and the AHC due to side jump is independent of σ_{xx} [9,13].

Currently, there is immense interest in the AHE due to its potential applications in spintronics such as for magnetic sensors and memory devices [17–19]. Several materials have been reported to have a large intrinsic AHC due to the Berry curvature originating from their characteristic spin-orbit coupled band structure. For example, the intrinsic AHC in Fe (751 S/cm) [14] and MnAs (∼10^3 S/cm) [13] has been reported to be due to the Berry curvature arising from a pair of spin-orbit coupled bands near the Fermi level. $Co_3Sn_2S_2$ [20], Fe_3Sn [21], and $LiMn_6Sn_6$ [22] show a large intrinsic AHC arising due to the finite Berry curvature associated with the band structure. Besides these materials, Heusler alloys [23–25] show exotic anomalous transport properties owing to the distinctive band structure due to the combined effect of SOI and broken time-reversal symmetry [15,26–28]. For example, Co_2MnAl [29], Co_2MnGa [26], and Fe_2-based Heusler alloys [30] show a large intrinsic AHE.

Co_2MnGa is a full Heusler compound that crystallizes in the $L2_1$ structure with space group $Fm\bar{3}m$, which has three nodal lines near the Fermi energy, derived from the three mirror symmetries present in the system in the absence of spin-orbit coupling (SOC) [31]. With the consideration of SOC, these nodal lines gap out according to the magnetization direction and create the large Berry curvature and intrinsic AHE in the system [28,31]. In this paper, we studied the AHE in the NiCoMnGa quaternary Heusler compound, which can be obtained by replacing the one Co atom by its neighboring Ni atom in the Co_2MnGa full Heusler

*ssingh.mst@iitbhu.ac.in

compound keeping the magnetic moments quite close for the two compounds. Experimentally, we found the value of the AHC to be around 256 S/cm at 10 K with an intrinsic contribution of ∼121 S/cm. The theoretical calculations give an intrinsic AHC of ∼100 S/cm, which is in good agreement with the experiment. The reduction of the mirror symmetries in NiCoMnGa in comparison to Co_2MnGa leads to the absence of nodal lines; nevertheless, the band splitting in the presence of SOC at the Fermi energy leads to the finite Berry curvature and intrinsic AHC in the system.

II. METHODS

The polycrystalline NiCoMnGa Heusler compound was synthesized by the arc-melting method in the environment of a high-pure-argon atmosphere using 99.99% pure constituent elements in a water-cooled copper hearth. To reduce further contamination, a Ti piece was used as an oxygen getter. The sample was flipped several times and remelted for homogeneous mixing. Energy-dispersive x-ray (EDX) analysis suggests a composition ratio of 1 : 1 : 1 : 1 within the standard deviation (3–5%) of the EDX measurement. For the structural analysis the x-ray diffraction (XRD) pattern of the powder sample was recorded at room temperature using a Rigaku-made x-ray diffractometer with Cu-K_α radiation. The magnetization measurements were performed using a vibrating sample magnetometer (VSM) attached to a physical property measurement system (PPMS) from Quantum Design. The resistivity and Hall measurements were carried out on a rectangular piece of sample of dimensions $4.34 \times 2.45 \times 0.66$ mm^3 employing the four-probe method using a cryogen-free measurement system (CFMS). The electronic band structure and magnetic properties of NiCoMnGa were calculated by employing density functional theory (DFT) using the Vienna *ab initio* simulation package (VASP) [32]. The generalized gradient approximation (GGA) of Perdew-Burke-Ernzerhof (PBE) type was used for the exchange-correlation functional [33]. A kinetic energy cutoff of 520 eV was taken for the plane-wave basis. A $15 \times 15 \times 15$ k-point mesh was used for the Brillouin zone (BZ) sampling, and the Gaussian smearing method with a width of 0.1 eV was adopted for the Fermi surface broadening. The cell parameter was relaxed until the forces on all atoms were smaller than 0.01 eV/Å. The SOC was taken into account in all the calculations. To explore the nontrivial band topology and the intrinsic AHC, a tight-binding Hamiltonian was constructed with the maximally localized Wannier functions using the WANNIER90 code [34,35]. Based on the tight-binding Hamiltonian, the AHC and the Berry curvature were evaluated via the Kubo-formula approach [36].

III. RESULTS AND DISCUSSION

A. Structure and magnetization

The XRD pattern of NiCoMnGa was recorded at room temperature for structural analysis. The observed XRD pattern [thin curve with red solid circles in Fig. 1(a)] fairly shows the cubic structure of the sample. The quaternary Heusler alloys generally crystallize in a LiMgPdSn-type structure (space group $F\bar{4}3m$) [37]. The Rietveld refinement of the room temperature XRD pattern of NiCoMnGa was carried out using the FULLPROF software package [38] with the space group $F\bar{4}3m$ (space group No. 216) and the following special Wyckoff positions: 4d (0.75, 0.75, 0.75), 4c (0.25, 0.25, 0.25, 0.25), 4b (0.5, 0.5, 0.5), and 4a (0, 0, 0) were considered for nickel (Ni), cobalt (Co), manganese (Mn), and gallium (Ga) atoms, respectively. The calculated XRD pattern (black curve) depicted in Fig. 1(a), shows that all the Bragg peaks are well indexed, which confirms the single phase (cubic) of the sample. The refined lattice parameter was found to be 5.79 Å, which matches well with the value reported in the literature [39]. The presence of the (111) and (200) superlattice reflections generally marks the ordered structure of Heusler compounds [15]. For NiCoMnGa the structure factors for the (111), (200), and (220) reflections can be written as [40]

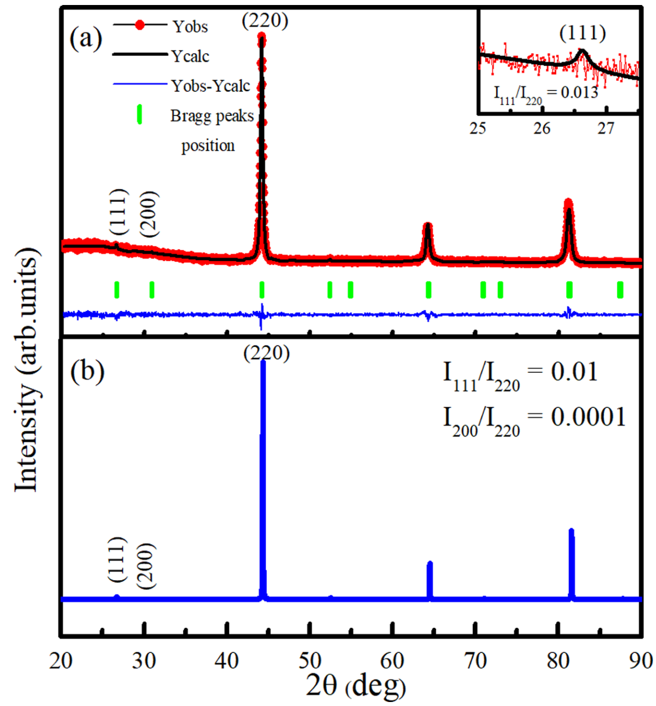

FIG. 1. (a) Rietveld refinement of the room temperature powder x-ray diffraction (XRD) data of the NiCoMnGa system. The inset shows an enlarged view of the XRD pattern around the (111) superlattice reflection. (b) Simulated XRD pattern of the NiCoMnGa system.

$$F_{111} = 4[(f_{\mathrm{Ga}} - f_{\mathrm{Mn}}) - i(f_{\mathrm{Ni}} - f_{\mathrm{Co}})], \quad (1)$$

$$F_{200} = 4[(f_{\mathrm{Ga}} + f_{\mathrm{Mn}}) - (f_{\mathrm{Ni}} + f_{\mathrm{Co}})], \quad (2)$$

$$F_{220} = 4[(f_{\mathrm{Ga}} + f_{\mathrm{Mn}}) + (f_{\mathrm{Ni}} + f_{\mathrm{Co}})]. \quad (3)$$

The negligible intensity of the (111) superlattice reflection survives only due to the difference of the atomic scattering factors (SFs) of Ga and Mn atoms as the difference between atomic SFs of Ni and Co atoms is negligible (they are consecutive elements in the periodic table) [15,40]. The vanishing intensity of the (200) reflection can be understood from Eq. (2). The intensity of the fundamental reflection is due to the sum of all the atomic SFs of the constituent elements

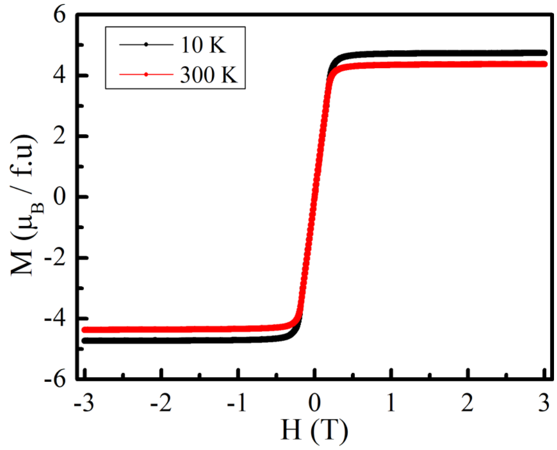

FIG. 2. Field-dependent magnetic isotherms at 10 and 300 K.

[Eq. (3)]. We simulated the XRD pattern of NiCoMnGa, depicted in Fig. 1(b), using POWDERCELL software [41]. The intensity ratio of the superlattice reflection (111) to the fundamental reflection (220) (i.e., $\frac{I_{111}}{I_{220}}$) was found to be about 0.01 and 0.012 from the simulated and observed XRD patterns, which suggests the formation of an ordered structure of the NiCoMnGa Heusler compound. The inset of Fig. 1(a) shows an enlarged view of the XRD pattern around the (111) superlattice reflection. Figure 2 shows the magnetic isotherms at temperatures 10 and 300 K. The magnetic moment was found to be 4.7 μ_B/f.u. at 10 K. The magnitude of the observed magnetic moment is close to the value reported in the literature [39].

B. Transport measurements

Figure 3(a) shows the measured temperature dependence of longitudinal resistivity ρ_{xx}. The temperature variation of ρ_{xx} indicates a metallic conduction with σ_{xx} of about 1.88×10^4 S/cm at 300 K. The residual resistance ratio [RRR = $\rho_{xx}(300\ \mathrm{K})/\rho_{xx}(10\ \mathrm{K})$], which quantifies the degree of disorder, is found to be around 2, which suggests a clean sample of NiCoMnGa [15]. Now, after investigating the phase purity, magnetization, and resistivity of the sample, we will discuss the outcome of the Hall measurements. The inset of Fig. 3(a) shows a schematic diagram of the sample device used for the longitudinal voltage V_{xx} and Hall voltage V_H measurements. In general the Hall resistivity ρ_H in magnetic materials is the sum of two parts [1,15]:

$$\rho_H = \rho_H^0 + \rho_H^A = R_0 H + R_s M. \tag{4}$$

ρ_H^0 and ρ_H^A are the ordinary and anomalous Hall resistivity, respectively. R_0, R_s, H, and M are the ordinary Hall coefficient, anomalous Hall coefficients, applied external magnetic field, and spontaneous magnetization of the material, respectively. R_0, which depends on the type of charge carriers and their density, is the inverse of the product of the carrier concentration n and electronic charge e [42]. The Hall resistivity in ferromagnetic materials is dominated by the AHE at lower field, and the role of the ordinary Hall effect usually appears in the higher-field region [15]. With the linear fitting of the high-field ρ_H

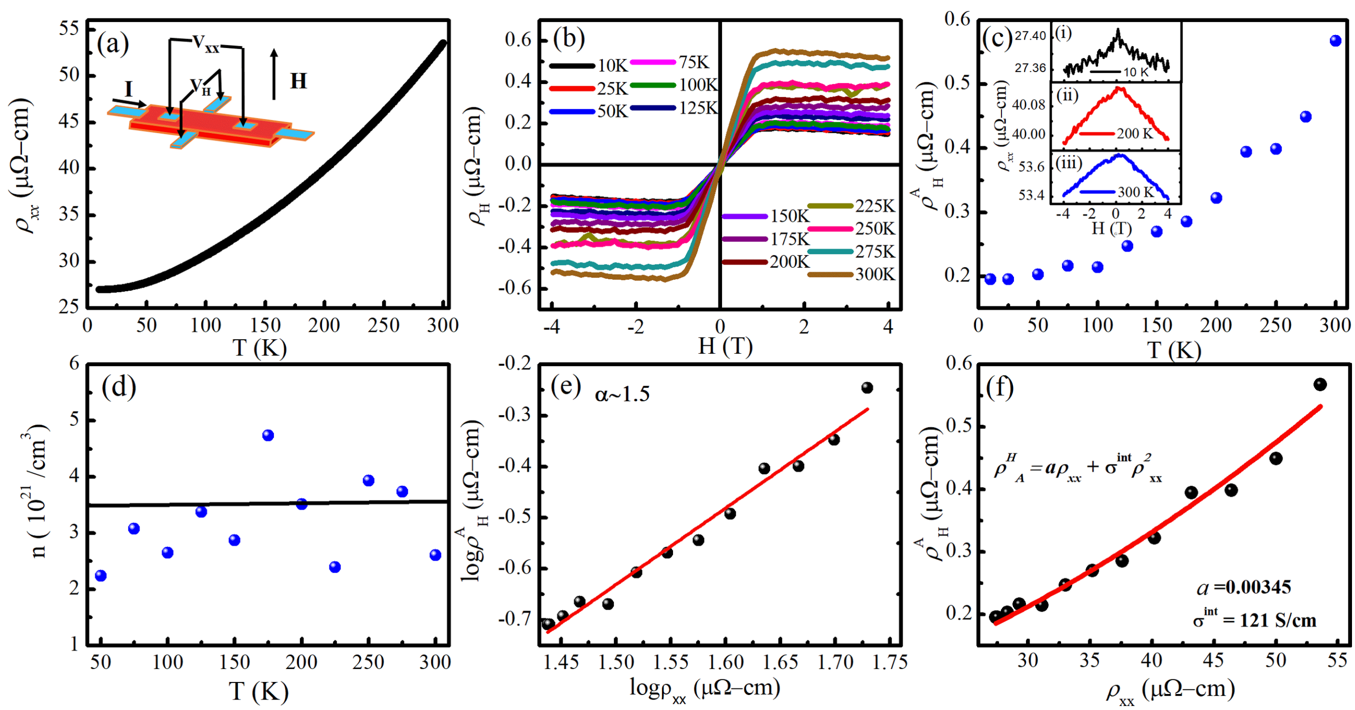

FIG. 3. (a) Temperature-dependent longitudinal resistivity ρ_{xx}. The inset shows a schematic drawing of the sample device used for Hall voltage V_H and longitudinal voltage V_{xx} measurements. (b) Field-dependent Hall resistivity ρ_H at different temperatures. (c) Temperature variation of the anomalous Hall resistivity ρ_H^A. The inset shows the field-dependent ρ_{xx} at (i) 10 K, (ii) 200 K, and (iii) 300 K. (d) Temperature-dependent carrier concentration n. (e) Double-logarithmic plot between ρ_H^A and ρ_{xx} (black balls); the linear fitting is shown by the red line. (f) ρ_H^A and ρ_{xx} plot (black balls); the fitted curve using Eq. (5) is shown in red.

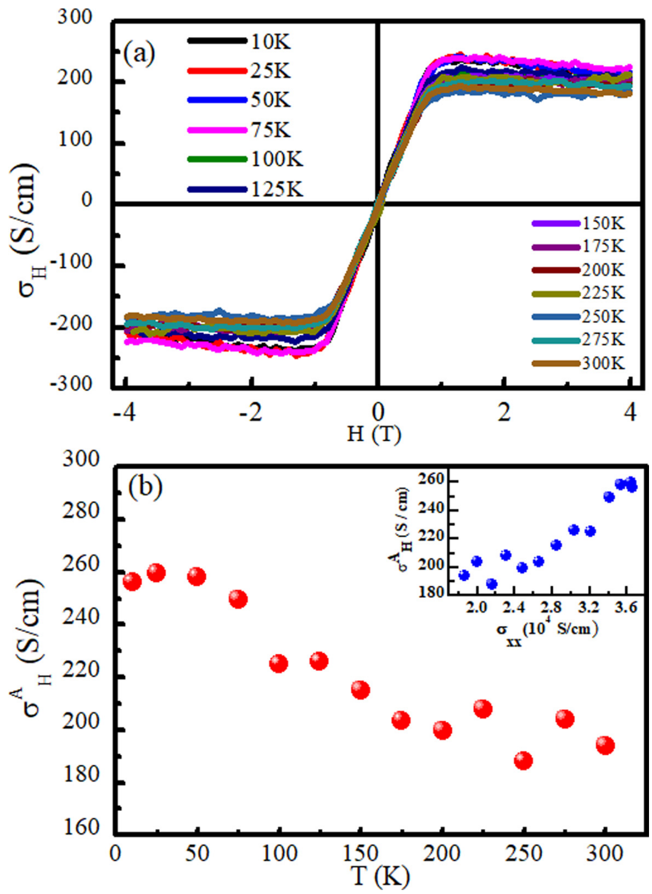

FIG. 4. (a) Field-dependent Hall conductivity σ_H at different temperatures. (b) Temperature variation of the anomalous Hall conductivity (AHC). The inset shows the variation of the AHC with longitudinal conductivity σ_{xx}.

curve, the slope and intercept on the y axis give R_0 and ρ_H^A, respectively. ρ_H^A is similar to the Hall response due to magnetization of the material in the absence of an external magnetic field. The Hall measurement outcomes are summarized in Figs. 3(b)–3(f) and Figs. 4(a) and 4(b). Figure 3(b) shows the field-dependent ρ_H isotherms up to a field of 4 T. The ρ_H curves show a sharp jump at low field and change linearly in the high-field regime, which signifies an AHE in the present material. Figure 3(c) displays the variation of extracted ρ_H^A with temperature. ρ_H^A increases nonlinearly with temperature and achieves a maximum value of about 0.56 $\mu\Omega$ cm at room temperature. We also measured the field-dependent ρ_{xx} at fixed temperatures. The ρ_{xx} does not change significantly with the magnetic field at a particular temperature as shown in the inset of Fig. 3(c) for (i) 10 K, (ii) 200 K, and (iii) 300 K. The charge carrier density n was calculated using the relation $R_0 = \frac{1}{ne}$ [42], and the temperature variation of n is depicted in Fig. 3(d). The magnitude of n is a little scattered with temperature and is estimated to be about 2.5×10^{21} cm^{-3} at 300 K. In order to examine the origin of the AHE, we have plotted ρ_H^A versus ρ_{xx} on a double-logarithmic scale as shown in Fig. 3(e). A linear fitting was done to determine the exponent α according to the formula $\rho_H^A \propto \rho_{xx}^\alpha$ [42,43]. If $\alpha = 1$, the origin of the AHE is due to skew scattering, and if $\alpha = 2$, the origin of the AHE is assigned to the intrinsic and side jump mechanisms [2,15,43]. In this way, we found the exponent $\alpha = 1.50$, which primarily specifies that the extrinsic and intrinsic mechanisms are involved in the AHE. To disentangle the intrinsic and extrinsic contributions linked with the AHE, we have used the following equation, which accounts for the phonon contribution in the skew scattering as suggested for alloy systems [15,42,44,45]:

$$\rho_H^A = a\rho_{xx} + \sigma^{\text{int}}\rho_{xx}^2. \tag{5}$$

Here, a is the parameter related to the skew scattering, and the notation σ^{int} is used for the intrinsic AHC. Here, we have assumed that the ratio of the SOI energy ϵ_{SO} to the Fermi energy E_F, i.e., ϵ_{SO}/E_F, is of the order of 10^{-3}–10^{-2}, which leads to the suppression of the side jump contribution in comparison to the intrinsic AHC as observed for other metallic ferromagnets [15,43]. Figure 3(f) shows a ρ_H^A versus ρ_{xx} plot (black balls), and the fitting was employed using Eq. (5) as shown by a red curve. From the fitting, the parameter a and σ^{int} come out to be 0.0034 and 121 S/cm, respectively. The change in σ_H^A with temperature and/or longitudinal conductivity σ_{xx} also holds the information about the mechanism involved in the AHE. The Hall conductivity σ_H was calculated using the equation [15,16,31]

$$\sigma_H = \frac{\rho_H}{\left(\rho_{xx}^2 + \rho_H^2\right)}. \tag{6}$$

Figure 4(a) shows the field-dependent Hall conductivity curves at different temperatures. The value of the AHC at a particular temperature is calculated by zero-field extrapolation of the high-field Hall conductivity data with the y axis. We found the AHC to be around 256 S/cm at 10 K. This value is nearly twice the magnitude of the intrinsic AHC, which shows the presence of equal contributions of the intrinsic and extrinsic AHC at 10 K. The AHC decreases with increasing temperature and reduces to 194 S/cm at 300 K as shown in Fig. 4(b). The variation of AHC with σ_{xx} is shown in the inset of Fig. 4(b). The decreasing (increasing) value of AHC with temperature (σ_{xx}) is due to the skew scattering contribution in AHC rather than the temperature variation of the spontaneous magnetization of the sample as the temperature has little effect on the magnetization of the present system (Fig. 2). It is worthwhile to mention here that the intrinsic AHE is expected to dominate in the overall behavior of the AHE, when the longitudinal conductivity of the sample lies in the good metallic regime, i.e., σ_{xx} is of the order of 10^4–10^6 S/cm [1,15,16,43,46]. Our system shows a deviation from this criterion as the extrinsic AHE has a significant contribution to the AHE despite the fact that σ_{xx} is of the order of 10^4 S/cm. The AHC due to skew scattering can be given as [47]

$$\sigma_H^{\text{skew}} = (\sigma_{xx})S = \frac{2e^2}{ha}\frac{E_F\tau}{\hbar}S, \tag{7}$$

where h, a, E_F, τ, and S are the Planck constant, lattice parameter, Fermi energy, mean free path of the electron, and skewness factor, respectively. The skewness factor is $S \sim \epsilon_{\text{SO}} v_{\text{imp}}/W^2$, where W is the bandwidth and v_{imp} is the impurity potential [47]. In the superclean limit where $\frac{\hbar}{\tau} \ll \epsilon_{\text{SO}}$, the skew scattering dominates; however, in the case of $\frac{\hbar}{\tau} < \epsilon_{\text{SO}}$,

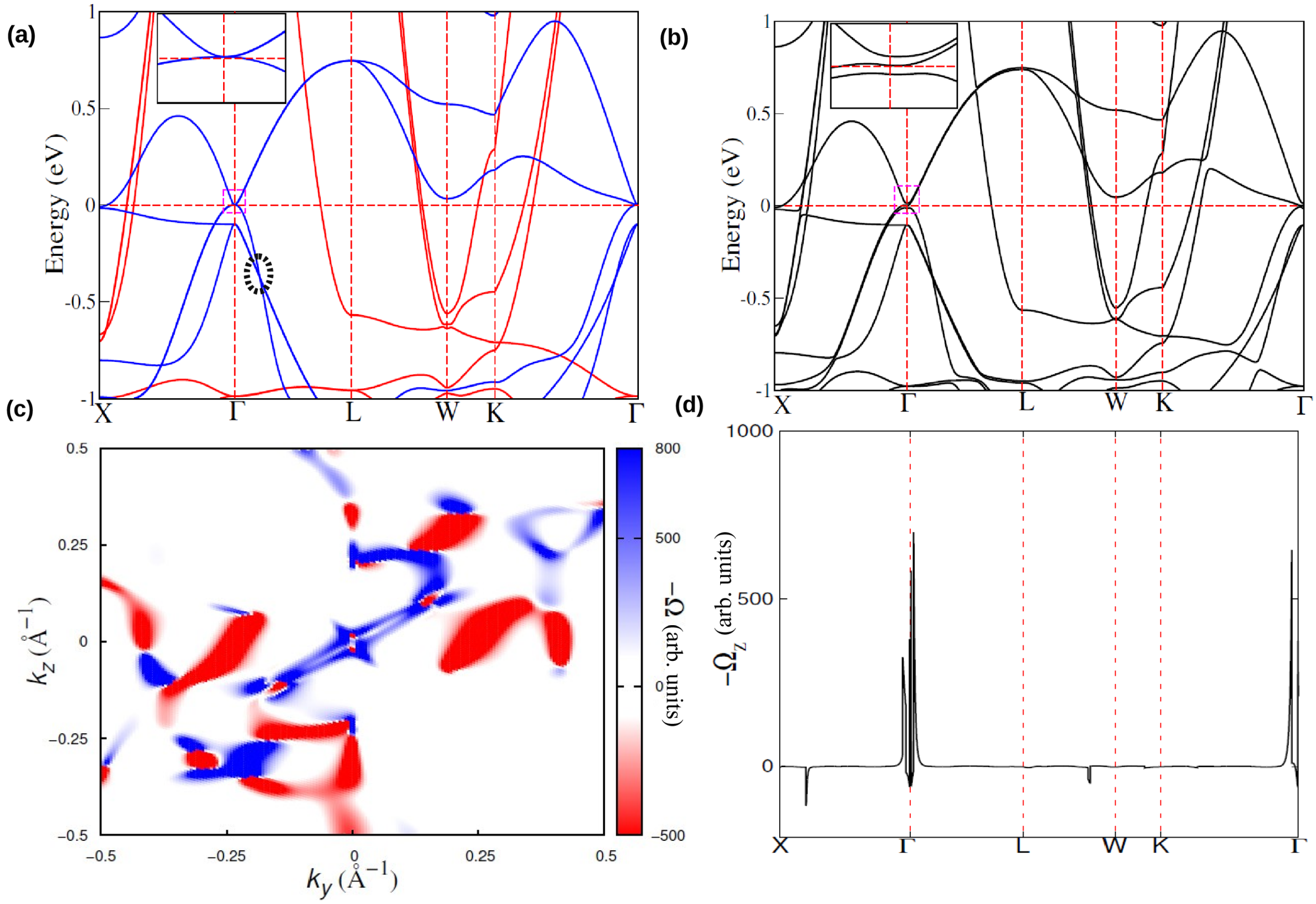

FIG. 5. (a) The band structure of NiCoMnGa in the absence of SOC, where the red and blue colors represent the spin-up and spin-down bands, respectively. (b) The band structure of NiCoMnGa in the presence of SOC. The inset shows the splitting of the bands near the Fermi energy E_F. (c) Berry curvature distribution in the k_y-k_z plane at $k_x = 0$. (d) Berry curvature along the high-symmetry path.

the skew scattering contribution decreases. From Eq. (7), it is clear that the skew scattering contribution rapidly decays with increasing $\frac{\hbar}{\tau}$. Henceforth, the value of the AHC due to skew scattering depends on both the strength of the SOI energy and the σ_{xx}. Our experiment also suggests that the lineup of the origin of the AHE based solely on the longitudinal conductivity is a rough estimation and need not be strictly valid. The intrinsic AHE depends on the Berry curvature of the system, which may have different origins such as the presence of a gapped nodal line, the presence of a Weyl point, or the presence of interband mixing along a certain high-symmetry path. Therefore, to understand the origin of the Berry curvature in the present system, we performed first-principles calculations.

C. First-principles calculations

The relaxed lattice parameter of NiCoMnGa was found to be 5.782 Å, which is consistent with the experiment. Our first-principles calculation for the magnetic moment suggests that Co and Mn have a large magnetic moment with $\mu_{\rm Co} = 1.188\ \mu_B/{\rm f.u.}$ and $\mu_{\rm Mn} = 3.246\ \mu_B/{\rm f.u.}$, respectively, whereas Ga has a small vanishing magnetic moment, and Ni has the moment $\mu_{\rm Ni} = 0.563\ \mu_B/{\rm f.u.}$ The total magnetic moment per formula unit is $4.993\ \mu_B$, aligned along the (001) direction, which is consistent with the Slater-Pauling rule for Heusler alloys [48]. To calculate the Berry curvature and the intrinsic AHE in the present system, a tight-binding Hamiltonian was constructed with the maximally localized Wannier functions [34,35]. Based on the tight-binding Hamiltonian, the AHC and the Berry curvature were evaluated via the Kubo-formula [36] approach in the linear response scheme as follows:

$$\sigma_{\alpha\beta} = -\frac{e^2}{\hbar}\sum_n \int \frac{d^3K}{(2\pi)^3}\Omega^n_{\alpha\beta} f_n, \tag{8}$$

where the Berry curvature Ω can be written as a sum over the eigenstate using the Kubo formula [11]

$$\Omega^n_{\alpha\beta} = i\sum_{n\neq n'} \frac{\langle n|\frac{\partial H}{\partial R^\alpha}|n'\rangle\langle n'|\frac{\partial H}{\partial R^\beta}|n\rangle - (\alpha \leftrightarrows \beta)}{(\epsilon_n - \epsilon'_n)^2}. \tag{9}$$

Here, $|n\rangle$ and ϵ_n are the energy eigenstate and eigenvalue of Hamiltonian H, respectively. f_n is the Fermi distribution function. The intrinsic AHE can be analyzed by exploring the electronic band structure of NiCoMnGa. Two major features in the electronic band structure make this system important. First, a twofold-degenerate band forms a triple-point crossing with a nondegenerate band along the high-symmetry direction Γ-L in the absence of SOC as shown in Fig. 5(a) by a black dotted circle. This doubly degenerate band splits in the pres-

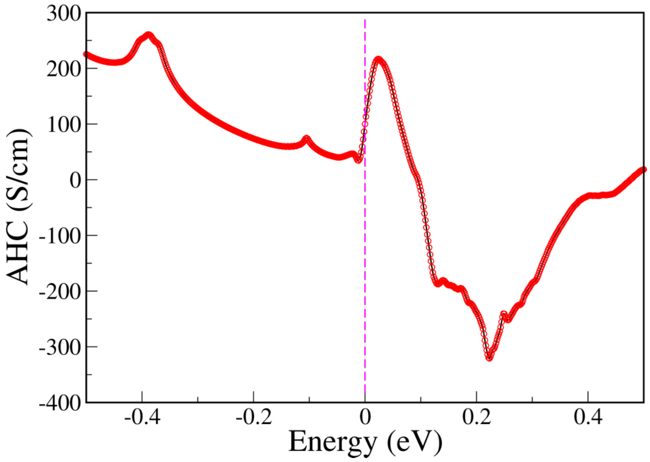

FIG. 6. Fermi energy scan of the anomalous Hall conductivity.

ence of SOC and also lifts the triple-point degeneracy. This degeneracy may arise due to a symmetry of C_{3v} along the Γ-L high-symmetry direction, whose elements are threefold rotation (C_3) and a σ_v mirror plane [49]. The second feature is a pair of degenerate minority spin bands at the Γ point in the absence of SOC; however, in the presence of SOC these bands split into an occupied band and an unoccupied band separated by a small energy gap in a small k interval near the Γ point as shown in Fig. 5(b). In Fig. 5(d), we calculated the Berry curvature Ω^z_{xy} in the presence of SOC along the same symmetry direction, and Ω^z_{xy} has a large value near the Γ point. This large value of the Berry curvature can be explained in terms of splitting of the degenerate band, which opens a small energy gap and creates intrinsic AHC in the system. Owing to the nearly degenerate conduction and valence band at Γ point, the Berry curvature is large at this point; therefore an intrinsic AHE is expected in the present compound. In Fig. 5(c), a color plot of the Berry curvature is shown in the $k_x = 0$ plane of the first Brillouin zone, which shows positive and negative distribution of the Berry curvature in the plane. Following the symmetry of the NiCoMnGa compound, if the magnetization is taken along the z axis, Ω^z_{xy} is the only surviving component of the Berry curvature. We found the intrinsic AHC due to finite Ω^z_{xy} to be about 100 S/cm at the Fermi level, which is consistent with the experiment (121 S/cm). We also show the dependency of the AHC as a function of the shift in the Fermi energy in Fig. 6, which gives an idea as to the contribution of various valence bands when shifting the Fermi energy. The large peak below the Fermi level (−0.38 eV) is due to the large Berry curvature at the triple point, which is contributing as an occupied valence band to the AHC. We observed the decreasing trend of the AHC from −0.38 eV, and it again increases at the Fermi energy due to a large positive Berry curvature, shown in blue in Fig. 5(c).

IV. CONCLUSIONS

We have experimentally measured the AHC in the NiCoMnGa quaternary Heusler compound and theoretically calculated the intrinsic part of the AHC due to the Berry curvature of the dispersion bands. The extrinsic and intrinsic mechanisms contribute equally to the AHC of the present system. We found a good agreement between the experimentally extracted intrinsic AHC and the theoretically calculated AHC. The reduction of the number of mirror symmetries in NiCoMnGa in comparison to Co_2MnGa leads to the absence of nodal lines; nevertheless, the band splitting in the presence of SOC at the Fermi energy leads to the finite Berry curvature and intrinsic AHC in the system. The presence of a signifisignificant contribution of the extrinsic mechanism in the AHE, despite the longitudinal conductivity being of the order of 10^4 S/cm, suggests that the relation of the origin of the AHE solely with the longitudinal conductivity may not be strictly valid.

ACKNOWLEDGMENTS

We gratefully acknowledge IIT BHU for experimental support. S.S. thanks the Science and Engineering Research Board of India for financial support through the "CRG" scheme (Grant No. CRG/2021/003256) and Ramanujan Fellowship (Grant No. SB/S2/RJN-015/2017) and UGC-DAE CSR, Indore, for financial support through the "CRS" scheme. G.K.S. acknowledges the DST-INSPIRE scheme for support through a fellowship. M.K. thanks DST for funding through Grant No. CRG/2020/000754. J.S. thanks the University Grants Commission (UGC) for support through a Ph.D. fellowship. V.K. thanks CSIR, New Delhi, for financial support.

[1] N. Nagaosa, Anomalous Hall effect–A new perspective, J. Phys. Soc. Jpn. **75**, 042001 (2006).

[2] N. Nagaosa, J. Sinova, S. Onoda, A. H. MacDonald, and N. P. Ong, Anomalous Hall effect, Rev. Mod. Phys. **82**, 1539 (2010).

[3] Y. Tian, L. Ye, and X. Jin, Proper Scaling of the Anomalous Hall Effect, Phys. Rev. Lett. **103**, 087206 (2009).

[4] D. Yue and X. Jin, Towards a better understanding of the anomalous Hall effect, J. Phys. Soc. Jpn. **86**, 011006 (2017).

[5] K. Manna, Y. Sun, L. Muechler, J. Kübler, and C. Felser, Heusler, Weyl and Berry, Nat. Rev. Mater. **3**, 244 (2018).

[6] J. Smit, The spontaneous Hall effect in ferromagnetics I, Physica **21**, 877 (1955).

[7] J. Smit, The spontaneous Hall effect in ferromagnetics II, Physica **24**, 39 (1958).

[8] R. Karplus and J. Luttinger, Hall Effect in Ferromagnetics, Phys. Rev. **95**, 1154 (1954).

[9] L. Berger, Side-jump mechanism for the Hall effect of ferromagnets, Phys. Rev. B **2**, 4559 (1970).

[10] G. Sundaram and Q. Niu, Wave-packet dynamics in slowly perturbed crystals: Gradient corrections and Berry-phase effects, Phys. Rev. B **59**, 14915 (1999).

[11] D. Xiao, M.-C. Chang, and Q. Niu, Berry phase effects on electronic properties, Rev. Mod. Phys. **82**, 1959 (2010).

[12] O. Stejskal, M. Veis, and J. Hamrle, The flow of the Berry curvature vector field, Sci. Rep. **12**, 97 (2022).

[13] C. Helman, A. Camjayi, E. Islam, M. Akabori, L. Thevenard, C. Gourdon, and M. Tortarolo, Anomalous Hall effect in MnAs: Intrinsic contribution due to Berry curvature, Phys. Rev. B **103**, 134408 (2021).
[14] Y. Yao, L. Kleinman, A. H. MacDonald, J. Sinova, T. Jungwirth, D.-s. Wang, E. Wang, and Q. Niu, First Principles Calculation of Anomalous Hall Conductivity in Ferromagnetic bcc Fe, Phys. Rev. Lett. **92**, 037204 (2004).
[15] G. K. Shukla, J. Sau, N. Shahi, A. K. Singh, M. Kumar, and S. Singh, Anomalous Hall effect from gapped nodal line in the Co_2FeGe Heusler compound, Phys. Rev. B **104**, 195108 (2021).
[16] G. K. Shukla, A. K. Jena, N. Shahi, K. K. Dubey, I. Rajput, S. Baral, K. Yadav, K. Mukherjee, A. Lakhani, K. Carva, S.-C. Lee, S. Bhattacharjee, and S. Singh, Atomic disorder and Berry phase driven anomalous Hall effect in a Co_2FeAl Heusler compound, Phys. Rev. B **105**, 035124 (2022).
[17] H. Ohno, D. Chiba, F. Matsukura, T. Omiya, E. Abe, T. Dietl, Y. Ohno, and K. Ohtani, Electric-field control of ferromagnetism, Nature (London) **408**, 944 (2000).
[18] D. Chiba, A. Werpachowska, M. Endo, Y. Nishitani, F. Matsukura, T. Dietl, and H. Ohno, Anomalous Hall Effect in Field-Effect Structures of (Ga,Mn)As, Phys. Rev. Lett. **104**, 106601 (2010).
[19] Q. Hao, W. Chen, S. Wang, and G. Xiao, Anomalous Hall effect and magnetic properties of Fe_xPt_{100-x} alloys with strong spin-orbit interaction, J. Appl. Phys. (Melville, NY) **122**, 033901 (2017).
[20] E. Liu, Y. Sun, N. Kumar, L. Muechler, A. Sun, L. Jiao, S.-Y. Yang, D. Liu, A. Liang, Q. Xu, J. Kroder, V. Süß, H. Borrmann, C. Shekhar, Z. Wang, C. Xi, W. Wang, W. Schnelle, S. Wirth, Y. Chen *et al.*, Giant anomalous Hall effect in a ferromagnetic kagome-lattice semimetal, Nat. Phys. **14**, 1125 (2018).
[21] T. Chen, S. Minami, A. Sakai, Y. Wang, Z. Feng, T. Nomoto, M. Hirayama, R. Ishii, T. Koretsune, R. Arita, and S. Nakatsuji, Large anomalous Nernst effect and nodal plane in an iron-based kagome ferromagnet, Sci. Adv. **8**, eabk1480 (2022).
[22] D. Chen, C. Le, C. Fu, H. Lin, W. Schnelle, Y. Sun, and C. Felser, Large anomalous Hall effect in the kagome ferromagnet $LiMn_6Sn_6$, Phys. Rev. B **103**, 144410 (2021).
[23] L. Wollmann, A. K. Nayak, S. S. Parkin, and C. Felser, Heusler 4.0: Tunable materials, Annu. Rev. Mater. Res. **47**, 247 (2017).
[24] T. Graf, C. Felser, and S. S. Parkin, Simple rules for the understanding of Heusler compounds, Prog. Solid State Chem. **39**, 1 (2011).
[25] K. Elphick, W. Frost, M. Samiepour, T. Kubota, K. Takanashi, H. Sukegawa, S. Mitani, and A. Hirohata, Heusler alloys for spintronic devices: Review on recent development and future perspectives, Sci. Technol. Adv. Mater. **22**, 235 (2021).
[26] K. Manna, L. Muechler, T.-H. Kao, R. Stinshoff, Y. Zhang, J. Gooth, N. Kumar, G. Kreiner, K. Koepernik, R. Car, J. Kübler, G.H. Fecher, C. Shekhar, Y. Sun, and C. Felser, From Colossal to Zero: Controlling the Anomalous Hall Effect in Magnetic Heusler Compounds via Berry Curvature Design, Phys. Rev. X **8**, 041045 (2018).
[27] S.-Y. Xu, I. Belopolski, N. Alidoust, M. Neupane, G. Bian, C. Zhang, R. Sankar, G. Chang, Z. Yuan, C.-C. Lee, S.-M. Huang, H. Zheng, J. Ma, D. S. Sanchez, B. Wang, A. Bansil, F. Chou, P. P. Shibayev, H. Lin, S. Jia *et al.*, Discovery of a Weyl fermion semimetal and topological Fermi arcs, Science **349**, 613 (2015).
[28] I. Belopolski, K. Manna, D. S. Sanchez, G. Chang, B. Ernst, J. Yin, S. S. Zhang, T. Cochran, N. Shumiya, H. Zheng, B. Singh, G. Bian, D. Multer, M. Litskevich, X. Zhou, S. M. Huang, B. Wang, T. R. Chang, S.-Y. Xu, A. Bansal *et al.*, Discovery of topological Weyl fermion lines and drumhead surface states in a room temperature magnet, Science **365**, 1278 (2019).
[29] P. Li, J. Koo, W. Ning, J. Li, L. Miao, L. Min, Y. Zhu, Y. Wang, N. Alem, C.-X. Liu, Z. Mao, and B. Yan, Giant room temperature anomalous Hall effect and tunable topology in a ferromagnetic topological semimetal Co_2MnAl, Nat. Commun. **11**, 3476 (2020).
[30] F. Mende, J. Noky, S. N. Guin, G. H. Fecher, K. Manna, P. Adler, W. Schnelle, Y. Sun, C. Fu, and C. Felser, Large anomalous Hall and Nernst effects in high Curie-temperature iron-based Heusler compounds, Adv. Sci. **8**, 2100782 (2021).
[31] S. N. Guin, K. Manna, J. Noky, S. J. Watzman, C. Fu, N. Kumar, W. Schnelle, C. Shekhar, Y. Sun, J. Gooth, and C. Felser, Anomalous Nernst effect beyond the magnetization scaling relation in the ferromagnetic Heusler compound Co_2MnGa, NPG Asia Mater. **11**, 16 (2019).
[32] J. Hafner, *Ab-initio* simulations of materials using VASP: Density-functional theory and beyond, J. Comput. Chem. **29**, 2044 (2008).
[33] P. E. Blöchl, Projector augmented-wave method, Phys. Rev. B **50**, 17953 (1994).
[34] G. Pizzi, V. Vitale, R. Arita, S. Blügel, F. Freimuth, G. Géranton, M. Gibertini, D. Gresch, C. Johnson, T. Koretsune, J. Ibañez-Azpiroz, H. Lee, J.-M. Lihm, D. Marchand, A. Marrazzo, Y. Mokrousov, J. I. Mustafa, Y. Nohara, Y. Nomura, L. Paulatto *et al.*, Wannier90 as a community code: New features and applications, J. Phys.: Condens. Matter **32**, 165902 (2020).
[35] N. Marzari and D. Vanderbilt, Maximally localized generalized Wannier functions for composite energy bands, Phys. Rev. B **56**, 12847 (1997).
[36] M. Gradhand, D. V. Fedorov, F. Pientka, P. Zahn, I. Mertig, and B. L. Györffy, First-principle calculations of the Berry curvature of Bloch states for charge and spin transport of electrons, J. Phys.: Condens. Matter **24**, 213202 (2012).
[37] D. Rani, Enamullah, K. G. Suresh, A. K. Yadav, S. N. Jha, D. Bhattacharyya, M. R. Varma, and A. Alam, Structural, electronic, magnetic, and transport properties of the equiatomic quaternary Heusler alloy CoRhMnGe: Theory and experiment, Phys. Rev. B **96**, 184404 (2017).
[38] J. Rodríguez-Carvajal, FULLPROF, a Rietveld and pattern matching and analysis program, version 2016, Laboratoire Léon Brillouin, CEA-CNRS, France, http://www.ill.eu/sites/fullprof/.
[39] V. Alijani, J. Winterlik, G. H. Fecher, S. S. Naghavi, and C. Felser, Quaternary half-metallic Heusler ferromagnets for spintronics applications, Phys. Rev. B **83**, 184428 (2011).
[40] Enamullah, Y. Venkateswara, S. Gupta, M. R. Varma, P. Singh, K. G. Suresh, and A. Alam, Electronic structure, magnetism, and antisite disorder in CoFeCrGe and CoMnCrAl quaternary Heusler alloys, Phys. Rev. B **92**, 224413 (2015).
[41] W. Kraus and G. Nolze, *POWDER CELL* – a program for the representation and manipulation of crystal structures and calculation of the resulting X-ray powder patterns, J. Appl. Crystallogr. **29**, 301 (1996).

[42] Q. Wang, Y. Xu, R. Lou, Z. Liu, M. Li, Y. Huang, D. Shen, H. Weng, S. Wang, and H. Lei, Large intrinsic anomalous Hall effect in half-metallic ferromagnet $Co_3Sn_2S_2$ with magnetic Weyl fermions, Nat. Commun. **9**, 3681 (2018).

[43] S. Roy, R. Singha, A. Ghosh, A. Pariari, and P. Mandal, Anomalous Hall effect in the half-metallic Heusler compound Co_2TiX (X = Si, Ge), Phys. Rev. B **102**, 085147 (2020).

[44] B. Ernst, R. Sahoo, Y. Sun, J. Nayak, L. Müchler, A. K. Nayak, N. Kumar, J. Gayles, A. Markou, G. H. Fecher, and C. Felser, Anomalous Hall effect and the role of Berry curvature in Co_2TiSn Heusler films, Phys. Rev. B **100**, 054445 (2019).

[45] V. L. Grigoryan, J. Xiao, X. Wang, and K. Xia, Anomalous Hall effect scaling in ferromagnetic thin films, Phys. Rev. B **96**, 144426 (2017).

[46] M. R. U. Nabi, A. Wegner, F. Wang, Y. Zhu, Y. Guan, A. Fereidouni, K. Pandey, R. Basnet, G. Acharya, H. O. H. Churchill, Z. Mao, and J. Hu, Giant topological Hall effect in centrosymmetric tetragonal $Mn_{2-x}Zn_xSb$, Phys. Rev. B **104**, 174419 (2021).

[47] S. Onoda, N. Sugimoto, and N. Nagaosa, Intrinsic Versus Extrinsic Anomalous Hall Effect in Ferromagnets, Phys. Rev. Lett. **97**, 126602 (2006).

[48] I. Galanakis, P. H. Dederichs, and N. Papanikolaou, Slater-Pauling behavior and origin of the half-metallicity of the full-Heusler alloys, Phys. Rev. B **66**, 174429 (2002).

[49] C. K. Barman, C. Mondal, B. Pathak, and A. Alam, Quaternary Heusler alloy: An ideal platform to realize triple point fermions, Phys. Rev. B **99**, 045144 (2019).